CORA Cork Open Research Archive
Cartlann Taighde Oscailte Chorcaí

Title	High-frequency radio polarization measurements of WMAP point sources
Authors	Jackson, N.;Browne, I. W. A.;Battye, R. A.;Gabuzda, Denise;Taylor, A. C.
Publication date	2010
Original Citation	Jackson, N., Browne, I. W. A., Battye, R. A., Gabuzda, D. and Taylor, A. C. (2010) 'High-frequency radio polarization measurements of WMAP point sources', Monthly Notices of the Royal Astronomical Society, 401(2), pp. 1388-1398. doi: 10.1111/j.1365-2966.2009.15757.x
Type of publication	Article (peer-reviewed)
Link to publisher's version	https://academic.oup.com/mnras/article-lookup/doi/10.1111/j.1365-2966.2009.15757.x - 10.1111/j.1365-2966.2009.15757.x
Rights	© 2009, the Authors. Journal compilation © 2009, RAS
Download date	2026-10-30 15:17:17
Item downloaded from	https://hdl.handle.net/10468/4967

UCC
University College Cork, Ireland
Coláiste na hOllscoile Corcaigh

Monthly Notices
of the
ROYAL ASTRONOMICAL SOCIETY

Mon. Not. R. Astron. Soc. **401,** 1388–1398 (2010) doi:10.1111/j.1365-2966.2009.15757.x

High-frequency radio polarization measurements of *WMAP* point sources

N. Jackson,[1⋆] I. W. A. Browne,[1] R. A. Battye,[1] D. Gabuzda[2] and A. C. Taylor[3]

[1] *Jodrell Bank Centre for Astrophysics, University of Manchester, Turing Building, Oxford Road, Manchester M13 9PL*
[2] *Physics Department, University College Cork, Cork, Ireland*
[3] *Oxford Astrophysics, University of Oxford, Denys Wilkinson Building, Keble Road, Oxford OX1 3RH*

Accepted 2009 September 19. Received 2009 September 11; in original form 2009 July 8

ABSTRACT

We present polarization measurements at 8.4, 22, and 43 GHz made with the Very Large Array (VLA) of a complete sample of extragalactic sources stronger than 1 Jy in the 5 yr *Wilkinson Microwave Anisotropy Probe* (*WMAP*) catalogue and with declinations north of -34°. The observations were motivated by the need to know the polarization properties of radio sources at frequencies of tens of GHz in order to subtract polarized foregrounds for future sensitive cosmic microwave background (CMB) experiments. The total intensity and polarization measurements are generally consistent with comparable VLA calibration measurements for less-variable sources, and within a similar range to *WMAP* fluxes for unresolved sources. A further paper will present correlations between measured parameters and derive implications for CMB measurements.

Key words: polarization – galaxies: active – radio continuum: galaxies.

1 INTRODUCTION

Radio source samples, selected at high frequency and with flux densities of the order of 1 Jy, mostly contain compact flat spectrum objects associated with the nuclei of active galaxies which have relativistic outflows pointing close to the direction of the observer (e.g. Blandford & Rees 1978; Scheuer & Readhead 1979; Orr & Browne 1982). This emission consists of a number of synchrotron components, each with a steep optically thin synchrotron spectrum at high frequencies and a self-absorbed spectrum at lower frequencies; the combination of many such components with different cut off frequencies produces the observed 'flat' radio spectrum. These components are frequently linearly polarized, and in principle useful information on jet physics can be obtained from the distribution of polarization in frequency and space. Although high-frequency-selected samples are dominated by flat spectrum objects, the samples do contain a minority of intrinsically more powerful sources in which the extended, steep-spectrum synchrotron emission dominates rather than the emission from a beamed core. Such sources also display linearly polarized emission, often at a higher level than the flat spectrum sources.

In recent years, there has been particular interest in high-frequency properties of radio sources because discrete radio sources act as a confusing foreground for measurements of the cosmic microwave background (CMB) (e.g. Tegmark & Efstathiou 1996). Such sources contribute most to the power spectrum on small angular scales (high ℓ), and efforts have been made to subtract their effects in several different ways. For total intensity, high-frequency observations of sources selected from lower frequency surveys have been used. For example, the Very Small Array CMB interferometer, working at 31 GHz, used 15 GHz source-finding observations with the Ryle Telescope followed by monitoring of discrete sources with dedicated long baselines (Dickinson et al. 2004) and/or single dish observations made with the Torun 32 m (Gawronski et al. 2009), while for the Cosmic Background Imager experiment high-frequency observations were made with the Owens Valley Radio Observatory (OVRO) 42 m and Green Bank Telescope (GBT) of sources selected at 1.4 GHz (Mason et al. 2003, 2009). Alternatively, population models based on extrapolations from lower frequency catalogues can be used statistically to ameliorate the effects of the extragalactic source foreground.

Although large-scale blind surveys at high frequencies are difficult to do, because of the small field of view at high frequencies, there are a number of both blind and pointed surveys in existence. The southern hemisphere has been completely surveyed by the AT20G survey (Ricci et al. 2004), which has been conducted with the Australia Telescope Compact Array (ATCA) at 18 GHz down to a limiting flux density of 50 mJy. A detailed study of brighter sources in this survey has been presented by Massardi et al. (2008). The whole sky has been covered to a brighter limiting flux density of about 1 Jy by *Wilkinson Microwave Anisotropy Probe* (*WMAP*) at a number of frequencies $\geq$20 GHz (Wright et al. 2009), and smaller areas of the northern sky have been covered to greater depth by surveys such as the 15 GHz 9C survey (Waldram et al. 2003). These surveys generally find that sources that are bright at high frequencies have complex spectra. About 30 per cent are significantly inverted (Ricci et al. 2004), and the mean spectral index around 20–40 GHz

⋆E-mail: neal.jackson@manchester.ac.uk

© 2009 The Authors. Journal compilation © 2009 RAS

tends to be around zero, generally steepening at higher frequencies (Ricci et al. 2006; Massardi et al. 2008; Vol'Vach et al. 2008). There is some evidence that the spectra of most sources turn over by 95 GHz (Sadler et al. 2008) but in general extrapolation to both higher frequencies and to lower flux density levels is needed in order to realistically simulate the CMB discrete foregrounds (e.g. Waldram et al. 2007). Importantly, there is convincing evidence that the mix of flat and steep spectrum sources changes with flux density. This is a prediction of beaming models (e.g. Orr & Browne 1982; Wall & Jackson 1997). There is also direct observational evidence provided by Gawronski et al. (in preparation) that the proportion of steep-spectrum sources with extended radio emission increases from $\leq$20 per cent in a *WMAP* 22 GHz sample to $\geq$50 per cent in Ryle-selected 15 GHz sample which has a flux density limit about two orders of magnitude weaker than that of the *WMAP* sample. Thus, care must be taken when extrapolating to both higher frequencies and lower flux densities. The sensitivity of instruments such as Planck require this to be done as accurately as possible, and hence it is important to base the models on as firm an observational footing as possible.

The situation with polarized foregrounds is less developed but it is becoming urgent to solve because inflation models make different predictions for the strength of B-modes in the CMB polarization distribution. A heroic effort is going into experiments to detect B-modes. These include Planck and ground-based projects like QUIET (Samtleben 2008) and the balloon-borne experiment SPIDER (Montroy et al. 2006). All CMB observations are technically challenging because they rely on extreme stability of the equipment and on meticulous subtraction of foregrounds to get at the true distribution of the CMB fluctuations. The detection of the B-mode signal will be particularly difficult (though just how difficult depends on its strength which varies over a wide range depending on the inflation model). For scalar-to-tensor ratio $r = 0.01$, the peak signal (at around 1° scales) is $\sim$30 nK. B-mode experiments operate at high frequencies (e.g. QUIET: 44 and 90 GHz; SPIDER: 90, 145 and 220 GHz; Planck: 30, 70, 100, 143, 217 and 353 GHz). Hence, observations at the highest frequencies possible are desirable. Estimates of synchrotron source total intensity contamination have been made by extrapolating from observations made at 1.4 and 5 GHz (e.g. Tucci et al. 2004). The current best-guess models are presented by Toffolatti et al. (1998, 2005). However, additional assumptions need to be made if the polarized foreground is to be characterized; one needs to know about the high-frequency polarization properties of sources. Ideally one would like direct observations of polarized source counts but this is impractical. An alternative is to use high-frequency total intensity source counts and a knowledge of how the percentage polarizations of sources change with both frequency and flux density to predict polarized source counts.

The work reported in this paper is the first phase in a programme aimed at improving knowledge about the polarization properties of radio sources at high radio frequencies. We begin with bright sources from the *WMAP* sample of Wright et al. (2009) which have $S_{22\,\mathrm{GHz}} > 1$ Jy. In this work, all but four of the samples of 203 *WMAP* sources with flux density of $\geq$1 Jy at 22 GHz and with declination $\delta > -34$ have been imaged with the Very Large Array (VLA) in total intensity and polarization. The second phase of our programme will be to measure the polarization properties of a high-frequency-selected sample of much weaker sources designed to look for any dependence of polarization properties on flux density. Given that Gawronski et al. (in preparation) find that the population mix changes with flux density, there is every reason to expect that average polarization properties also change.

2 OBSERVATIONS AND DATA REDUCTION

Observations were conducted using the VLA in D-configuration between 01.40 and 19.30 UT on 2008 August 1. During this period, 16 antennae were equipped with expanded VLA (EVLA) receivers while the remaining 11 had original VLA receivers. Each source was normally observed at three frequencies: two 50 MHz bands centred on 8.4351 and 8.4851 GHz (*X* band), two 50 MHz bands centred on 22.4351 and 22.4851 GHz (*K* band), and two 50 MHz bands centred on 43.3149 and 43.3649 MHz (*Q* band). Pointing calibration was carried out approximately every 15–20 min. The available time allowed observations to be made of all the sources at 22 and 43 GHz, and approximately two-thirds of the sources at 8 GHz. Four sources (*WMAP* 0823+224, *WMAP* 0824+392, *WMAP* 1014+231 and *WMAP* 1840+797) were missed during the observations, leaving a total of 199 sources out of 203 with attempted measurements. The source 3C48 was observed in order to provide an additional flux and polarization calibrator; the primary flux and polarization calibrator, 3C286 (*WMAP* 1331+305), was already part of the sample. Additionally, three much weaker sources from the 9C survey were also observed as a pilot for a future observing programme aimed at much weaker sources.

The nominal time on each source was 37 s at 8 GHz, 30 s at 22 GHz and 80 s at 43 GHz, giving a theoretical rms of 0.2, 0.5 and 0.7 mJy beam^{-1}, respectively, for natural weighting. However, the rms noise in most images is typically greater than this, being between 1 mJy beam^{-1} and 2 mJy beam^{-1} in the majority of images. This is partly due to the use of uniform weighting during the imaging process, which increases the noise level typically by factors between 1.2 and 1.5. However, in particular, 8-GHz observations were affected by a combination of missing antennae and slightly longer than predicted slew and setup times on many sources. A sampling time of 3 s per integration was used, the minimum allowed by the observing system.

All data analysis and processing was carried out in the AIPS package, distributed by the US National Radio Astronomy Observatory. Data were examined and flagged manually. The 22 GHz data were relatively clean, but extensive flagging of bad telescopes was performed source by source on both 8 and 43 GHz data, resulting in the removal of up to half of the data on any given source. The major problems were loss of correlation on some telescopes during setup at the beginning of a scan and intermittent bad data on many individual telescopes.

Overall amplitude calibration was performed using observations of the source 3C286 at each frequency and normalizing to the flux scale of Baars et al. (1977). Amplitude and phase solutions were made using the sources stronger than a limiting flux density; the process was iterated, adjusting this limiting flux, until the amplitude and phase solutions appeared to vary in a coherent manner. Amplitude solutions were smoothed using an averaging time of 1 h for 43 GHz and 0.1 h for the other frequencies. In the case of the 8 GHz observations, a further calibration was made, again using a standard model for 3C286, for baseline-dependent offsets. This was necessary because of the mixture of receivers in the array, approximately equally distributed between old (VLA) and new (EVLA) receivers.

Polarization calibration was then carried out. Telescope polarization offsets were calibrated by use of the source 3C84, which was assumed to have zero polarization. This assumption is correct for the level of accuracy required here: Taylor et al. (2006) report levels of $<$0.1 per cent polarization in the core of the source at frequencies less than 22 GHz, with approximately 0.2 per cent at 22 GHz, and a

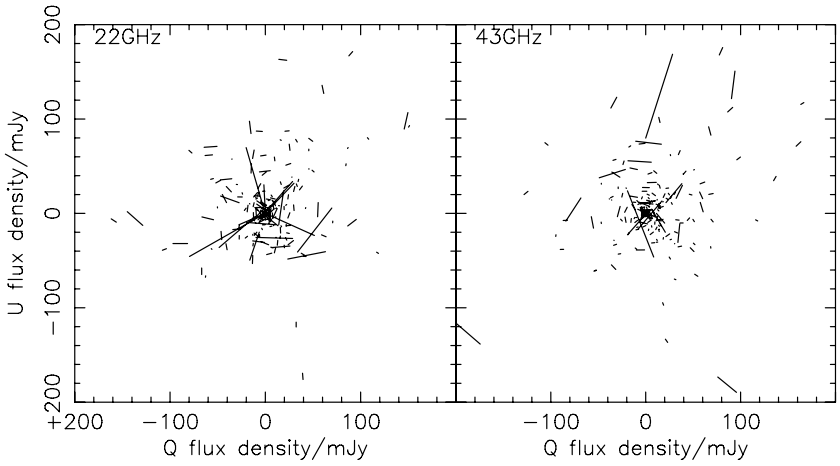


Figure 1. Estimates of the Stokes parameters Q and U for the mapped sources, in mJy, for the two methods described in the text [fitting to the images and to the (u, v) data]. In each case, Q, in mJy, is the abscissa and U, in mJy, is the ordinate, and lines on the plot join the (Q, U) coordinates of the first measurement to those of the second. Note that for most sources the methods agree well and the lines are relatively short. In cases of disagreement, we provide a note in Table 2 explaining the choice of polarized flux densities used in the data tables.

Table 1. Average intensity and polarization quantities for the sample, counting polarization limits as zero.

Frequency (GHz)	1.4	1.4–8.4	8.4	8.4–22	22	22–43	43
Polarization (per cent)	2.2 ± 0.2 (1.6)		3.1 ± 0.2 (2.6)		2.7 ± 0.2 (2.2)		3.1 ± 0.2 (2.6)
Intensity spectral index		0.01 ± 0.04 (0.04)		-0.20 ± 0.05 (-0.15)		-0.49 ± 0.04 (-0.37)	
Polarization spectral index		0.35 ± 0.07 (0.28)		0.01 ± 0.10 (-0.15)		-0.09 ± 0.06 (-0.14)	

Note. 1.4 GHz observations are from NVSS, 8.4 GHz observations from CLASS and this work, and the remainder from this work. Median values are given in brackets. Spectral indices are defined as $S_\nu = \nu^\alpha$.

somewhat higher level (0.8–7.5 per cent) in the weak mas-scale jet component. The overall level of polarization in 3C84 is likely to be about 0.1 per cent. 3C84 was not observed at 8 GHz. In this case, the source 0125−001, a bright point source for which no significant polarization was detected in either 22 GHz or 43 GHz observations, was used instead. The polarization position angle was calibrated by use of the 3C286 data, applying corrections to the R–L phase difference to rotate the 3C286 polarization position angle to 33°. The baseline-to-baseline scatter in this quantity was 0°.6, 3°.3 and 8°.5 for 8, 22 and 43, respectively.

Imaging was performed using the AIPS task IMAGR with uniform weighting, on a default 128×128 grid and cellsizes of 1.8, 0.7 and 0.35 arcsec for 8, 22 and 43, respectively. For strong sources (roughly speaking, those containing sufficient flux density to have been used as phase calibrators), one iteration of phase-only self-calibration and one iteration of amplitude self-calibration were applied. Final total intensity images were produced using 1000 CLEAN iterations (Högbom 1974); images in Stokes Q and U were produced using a limited number (40) of iterations to avoid reduction in the signal due to CLEAN bias (e.g. Condon et al. 1998).

Estimation of the Stokes I, Q and U flux densities was performed in two ways. The first method consisted of fitting to the calibrated (u, v) data, constraining the fit by fixing the position to the peak of the I map, constraining the intrinsic size of the peak component to be $<1''$, but allowing the Q and U flux density to vary. Constraints are necessary to avoid instability in the fits due to noise in the polarization data. The alternative method consisted of finding, and fitting to, the highest absolute value in the Q and U images, within a square of side 10 pixels. Neither method is ideal. Fitting to the (u, v) data has the advantage of independence from effects due to deconvolution, notably the effects of CLEAN bias. On the other hand, stabilizing the fit requires fixing the peak of the Stokes Q and U to the peak of the I data, and this may not be appropriate for sources with extended polarized structure. Fig. 1 shows a comparison of the two methods, and demonstrates that for the majority of sources the two methods agree well. Approximately, 10 per cent of sources show significant disagreement, mostly those with low polarized flux densities. Table 1 shows average results for all objects in the sample. In Table 2, where the data are presented, detailed comments are given in cases where the two methods disagree. Errors given in Table 2 are a quadrature combination of the random error, as output by AIPS, and the systematic calibration error, assumed to be 5 per cent for 43 and 22 GHz and 2 per cent at 8.4 GHz.

Because the total polarization is a quadratic sum of Q and U, it is positive-biased; values of polarized flux density of three times the rms noise cannot therefore be regarded as significant detections. Many studies of this effect have been made. For example, Simmons & Stewart (1985) give a relation of estimated signal-to-noise ratio, p_o, and observed signal-to-noise ratio p, in polarization for four different indicators. These all converge towards equality for $p > 4$ as $p_o = (p^2 - 1)^{1/2}$, and diverge strongly for $p < 2$, reaching values of $1 < p < 1.5$ for $p_o = 0$. The issue in these observations is complicated by the different values of rms noise in different images.

© 2009 The Authors. Journal compilation © 2009 RAS, MNRAS **401,** 1388–1398

Table 2. Flux densities of observed sources at *X*, *K* and *Q* bands.

	X band			*K* band			*Q* band			
	I (mJy)	*P* (mJy)	Angle (°)	*I* (mJy)	*P* (mJy)	Angle (°)	*I* (mJy)	*P* (mJy)	Angle (°)	
0006 − 063	2100 ± 40	20.5 ± 0.4	155.9 ± 0.5	1820 ± 90	65.4 ± 2.5	22.8 ± 1.1	1540 ± 80	52.5 ± 2.5	10.9 ± 0.9	
0010 + 110	*469.0 ± 0.1*	*0.2 ± 0.1*	*87 ± 7*	710 ± 40	6.3 ± 2.4†	115 ± 10	1550 ± 80	13.4 ± 1.3	29 ± 3	
0019 + 203	*1275.1 ± 0.4*	*55.8 ± 0.2*	*106.9 ± 0.1*	650 ± 30	7.1 ± 1.9†	149 ± 12	475 ± 24	<10	–	
0019 + 260	389 ± 8	8.1 ± 0.2	9.4 ± 0.7	347 ± 17	<10	–	270 ± 14	<10	–	1
0029 + 059	740 ± 15	19.8 ± 0.3	116.0 ± 0.5	630 ± 30	17.5 ± 2.0	130 ± 4	423 ± 21	15.9 ± 1.3	146.9 ± 2.6	
0043 + 521				179 ± 11	<10	–	46.7 ± 2.9	<10	–	2
0047 − 252				268 ± 16	<10	–	73 ± 8	<10	–	3
0050 − 068	940 ± 19	23.0 ± 0.5	144.8 ± 0.4	1370 ± 70	36 ± 3	145 ± 5	1320 ± 70	39.1 ± 2.1	127.9 ± 1.2	
0051 − 094				1480 ± 70	62.6 ± 2.8	156.6 ± 1.3	1470 ± 70	77 ± 3	147.2 ± 0.9	4
0108 + 015	1620 ± 30	66.0 ± 1.0	112.9 ± 0.5	1980 ± 100	38.2 ± 2.4	103.3 ± 1.3	1670 ± 80	29.1 ± 2.0	115.3 ± 2.2	
0108 + 133	900 ± 27	78.4 ± 1.8	95.8 ± 0.3	39.5 ± 2.3	<10	–	28.9 ± 1.9	<10	–	5
0116 − 116	912 ± 18	19.0 ± 0.4	105.6 ± 0.5	910 ± 50	<10	–	960 ± 50	13.1 ± 1.3	171.1 ± 2.2	
0121 + 118	3810 ± 80	59.0 ± 1.2	90.3 ± 0.1	3130 ± 160	178 ± 7	15.8 ± 0.9	1990 ± 100	143 ± 7	8.0 ± 0.6	
0125 − 001	1089 ± 22	<10	–	1030 ± 50	<10	–	780 ± 40	4.7 ± 2.1†	111 ± 14	6
0132 − 168	830 ± 17	18.0 ± 0.4	104.5 ± 0.6	1250 ± 60	13 ± 6†	11 ± 6	1660 ± 80	39.4 ± 2.1	164.1 ± 1.4	7
0137 − 244	949 ± 19	19.1 ± 0.4	113.3 ± 0.6	910 ± 50	<10	–	690 ± 30	16.8 ± 2.0	12 ± 3	
0137 + 478	3140 ± 60	26.6 ± 0.6	116.3 ± 0.5	2660 ± 130	59.1 ± 3.0	71.5 ± 1.3	1750 ± 90	19.1 ± 1.4	58.5 ± 2.3	
0149 + 058	1137 ± 23	25.4 ± 0.4	112.7 ± 0.5	730 ± 40	<10	–	421 ± 21	<10	–	
0152 + 221	*1038.5 ± 0.1*	*20.9 ± 0.1*	*56.8 ± 0.1*	890 ± 40	42.4 ± 2.4	3.5 ± 0.8	730 ± 40	46.5 ± 2.5	177.1 ± 0.9	8
0204 + 152	1485 ± 30	30.1 ± 0.6	142.1 ± 0.3	820 ± 40	6.3 ± 1.0†	58 ± 5	547 ± 27	18.8 ± 1.3†	168.9 ± 1.9	
0205 + 322	*626.8 ± 2.3*	*5.2 ± 0.1*	*48.4 ± 0.4*	3060 ± 150	102 ± 6	99.1 ± 0.7	2150 ± 110	87 ± 4	92.4 ± 0.6	
0218 + 016	*1209.5 ± 0.7*	*17.7 ± 0.3*	*149.7 ± 0.4*	1720 ± 90	20.1 ± 1.6	5.7 ± 1.9	1690 ± 80	31.8 ± 1.5	19.0 ± 1.3	
0220 + 359	1720 ± 30	134.2 ± 2.4	35.8 ± 0.2	1400 ± 70	194 ± 8	31.0 ± 0.8	950 ± 50	145 ± 5	25.4 ± 1.0	
0223 + 430	231 ± 6	9.5 ± 0.5	170.3 ± 1.1	152 ± 8	<10	–	94 ± 6	<10	–	9
0231 + 133	*1732.2 ± 1.4*	*11.5 ± 0.2*	*157.0 ± 0.6*	1390 ± 70	9.4 ± 1.3†	157 ± 4	1030 ± 50	11.1 ± 1.8†	117 ± 4	
0237 + 288	3640 ± 70	144.8 ± 2.1	67.6 ± 0.4	3050 ± 150	49.3 ± 2.6	78.0 ± 1.2	2380 ± 120	47.9 ± 1.9	112.4 ± 1.2	
0238 + 166	3190 ± 60	30.8 ± 0.7	91.7 ± 0.3	3340 ± 170	85 ± 4	34.0 ± 0.8	3160 ± 160	57.7 ± 2.3	23.2 ± 1.1	
0241 − 083				1060 ± 50	<10	–	960 ± 50	11.3 ± 1.2	140.0 ± 2.7	10
0259 − 002	1067 ± 21	25.5 ± 0.4	116.5 ± 0.5	860 ± 40	14.0 ± 2.4	55 ± 3	508 ± 25	<10	–	
0308 + 040	833 ± 21	29.3 ± 0.8	105.0 ± 0.6	542 ± 27	6.4 ± 1.1†	63 ± 5	372 ± 19	6.1 ± 1.1†	116 ± 5	11
0309 + 104	*1243.1 ± 1.1*	*25.9 ± 0.3*	*124.5 ± 0.3*	810 ± 40	33.9 ± 2.1	74.5 ± 1.6	760 ± 40	34.1 ± 1.6	63.9 ± 1.4	
0319 + 415				14530 ± 730	12 ± 3	99 ± 7	10620 ± 530	51 ± 5	57.3 ± 1.8	12
0329 − 239	1137 ± 23	35.3 ± 0.6	157.0 ± 0.5	1250 ± 60	13.2 ± 1.5	104 ± 4	1040 ± 50	11.2 ± 1.9	110 ± 5	
0336 − 129				453 ± 23	11.4 ± 1.7	171 ± 7	399 ± 20	13.5 ± 1.3	163.6 ± 2.7	
0339 − 017				2040 ± 100	67 ± 4	91.6 ± 0.4	1780 ± 90	48.0 ± 2.5	96.5 ± 1.1	
0340 − 213	1054 ± 21	26.9 ± 0.6	132.3 ± 0.4	900 ± 50	14 ± 3	39 ± 4	720 ± 40	14.6 ± 1.4	30.3 ± 2.9	
0348 − 277				760 ± 40	46 ± 4	41.8 ± 1.5	760 ± 40	41.8 ± 2.6	43 ± 5	
0358 + 104	75 ± 4	18.2 ± 0.5	103.4 ± 0.8	6.7 ± 1.1	<10	–	6.4 ± 1.1	<10	–	13
0405 − 130	2230 ± 40	31.1 ± 0.6	157.9 ± 0.5	1300 ± 70	68 ± 4	169.4 ± 1.0	850 ± 40	22.4 ± 2.3	166.4 ± 2.3	14
0411 + 769	2060 ± 40	48.9 ± 0.8	120.4 ± 0.4	1060 ± 50	71 ± 4	176.7 ± 0.9	570 ± 29	44.2 ± 1.9	156.6 ± 1.2	
0416 − 208	1103 ± 23	40.7 ± 0.8	121.8 ± 0.4	650 ± 30	11.8 ± 2.1†	52 ± 5	544 ± 27	<10	–	
0423 − 013	3920 ± 80	157.9 ± 3.0	97.6 ± 0.2	4340 ± 220	145 ± 8	89.6 ± 0.3	3710 ± 190	130 ± 6	85.6 ± 0.6	
0423 + 023	266 ± 5	5.6 ± 0.3	126.0 ± 2.4	201 ± 10	7.3 ± 0.9	124 ± 4	113 ± 6	7.2 ± 1.3	116 ± 5	15
0424 + 005	518 ± 10	21.7 ± 0.5	88.0 ± 0.4	481 ± 24	20.0 ± 1.8	60.4 ± 2.2	411 ± 21	20.4 ± 1.6	43.0 ± 1.9	
0433 + 053	3660 ± 70	90.1 ± 1.7	144.0 ± 0.3	2650 ± 130	126 ± 6	170.2 ± 0.7	1950 ± 100	86 ± 3	154.7 ± 1.0	
0453 − 281	1960 ± 40	43 ± 8	123.8 ± 2.4	1700 ± 90	21 ± 5	63 ± 5	1440 ± 70	14.1 ± 2.5	11 ± 6	
0456 − 233	2080 ± 40	44.7 ± 1.1	120.3 ± 0.6	1950 ± 100	11.7 ± 2.3†	117 ± 5	1530 ± 80	18.4 ± 2.7†	106 ± 4	16
0501 − 019	995 ± 20	8.3 ± 0.3	109.7 ± 0.9	960 ± 50	6.3 ± 1.1	33 ± 6	890 ± 40	33.6 ± 1.8	34.1 ± 1.0	
0513 − 219	1041 ± 21	7.5 ± 0.6	122.1 ± 1.7	800 ± 40	43.7 ± 2.8	136 ± 4	620 ± 30	38.7 ± 2.6	134.1 ± 1.2	
0519 − 056	8.1 ± 0.3	<10	–	3.8 ± 1.4	<10	–	2.6 ± 0.9	<10	–	17
0527 − 126				470 ± 50	<10	–	104 ± 13	<10	–	18
0542 + 498	4680 ± 90	119.9 ± 2.1	168.9 ± 0.3	1820 ± 90	67.8 ± 2.8	73.9 ± 1.0	820 ± 40	41.4 ± 2.1	79.1 ± 1.0	
0555 + 397	*7200 ± 18*	*51.8 ± 0.1*	*64.4 ± 0.1*	3110 ± 160	21.6 ± 1.7	158.4 ± 2.3	2040 ± 100	32.9 ± 1.7	151.9 ± 1.4	19
0607 + 673	*611.5 ± 0.4*	*21.5 ± 0.3*	*121.8 ± 0.3*	600 ± 30	<10	–	435 ± 23	49 ± 18†	20 ± 11	
0608 − 223	1376 ± 28	28.8 ± 0.7	89.2 ± 0.4	1470 ± 70	68 ± 4	50.0 ± 2.2	1150 ± 60	74 ± 4	45.3 ± 0.8	
0609 − 156				2990 ± 150	54 ± 5	52.8 ± 1.4	2190 ± 110	40 ± 6	68 ± 4	
0629 − 199	682 ± 14	8.8 ± 0.3	53.4 ± 0.9	610 ± 30	7.9 ± 1.7†	27 ± 6	407 ± 20	9.2 ± 1.9†	173 ± 13	
0636 − 205	283 ± 8	42.0 ± 1.0	116.6 ± 0.7	34.9 ± 2.9	<10	–	9.2 ± 2.1	<10	–	20
0646 + 448	3800 ± 80	84.7 ± 1.7	44.8 ± 0.1	3160 ± 160	21.8 ± 1.3	122.9 ± 1.5	2120 ± 110	31.9 ± 2.0	140.6 ± 1.8	
0721 + 713	2070 ± 40	67.1 ± 1.4	180.0 ± 0.1	4050 ± 200	91 ± 12	28 ± 6	4680 ± 230	127 ± 6	52.0 ± 0.5	
0738 + 177	891 ± 18	15.6 ± 0.4	147.4 ± 0.8	640 ± 30	21.0 ± 1.9	160.7 ± 2.3	407 ± 20	14.9 ± 1.9	155 ± 4	
0739 + 016	*1809.3 ± 0.9*	*58.9 ± 0.3*	*45.1 ± 0.1*	1520 ± 80	45.1 ± 2.3	22.0 ± 1.5	1480 ± 70	29.6 ± 1.8	9.4 ± 1.2	

© 2009 The Authors. Journal compilation © 2009 RAS, MNRAS **401,** 1388–1398

Table 2 – *continued*

	X band			*K* band			*Q* band			
	I (mJy)	*P* (mJy)	Angle (°)	*I* (mJy)	*P* (mJy)	Angle (°)	*I* (mJy)	*P* (mJy)	Angle (°)	
0741 + 311	1610 ± 30	79.2 ± 1.5	36.9 ± 0.2	760 ± 40	19.1 ± 3.0	74 ± 7	458 ± 23	17.8 ± 1.3	68.9 ± 2.0	
0745 + 102				970 ± 50	10.3 ± 1.5†	14 ± 3	312 ± 16	<10	–	21
0746 − 007	1910 ± 40	65.7 ± 1.3	93.7 ± 0.2	1060 ± 50	27.9 ± 1.5	147.1 ± 1.3	567 ± 28	18.4 ± 1.5	139 ± 7	
0750 + 125	4810 ± 110	129.7 ± 1.9	69.4 ± 0.4	4230 ± 210	148 ± 7	33.2 ± 0.8	2800 ± 140	113 ± 4	27.1 ± 1.0	
0753 + 539	967 ± 19	103.2 ± 1.8	34.2 ± 0.3	1020 ± 50	91 ± 4	37.0 ± 0.7	910 ± 50	76 ± 3	30.7 ± 1.0	
0757 + 099	1118 ± 22	47.5 ± 1.0	46.7 ± 0.2	1010 ± 50	50.3 ± 2.4	23.0 ± 1.3	750 ± 40	38.6 ± 1.7	17.8 ± 1.2	
0808 − 078				710 ± 40	15.3 ± 2.0	43 ± 10	700 ± 30	23.5 ± 1.6	43.6 ± 1.1	
0813 + 482	1960 ± 60	24.9 ± 0.5	11.9 ± 0.5	440 ± 40	12.0 ± 1.1	134.4 ± 2.2	172 ± 16	6.1 ± 0.8	119 ± 4	22
0825 + 031	1218 ± 24	84.3 ± 1.5	54.6 ± 0.3	1460 ± 70	78 ± 4	35.6 ± 0.9	1340 ± 70	45.9 ± 2.6	39.8 ± 0.7	
0831 + 241	–	–	–	–	–	–	1360 ± 70	35.8 ± 2.4†	13.2 ± 2.0	23
0836 − 202	2730 ± 50	70.3 ± 1.0	111.3 ± 0.4	1790 ± 90	44 ± 3†	23.4 ± 2.0	1020 ± 50	9.1 ± 1.3†	161 ± 4	24
0838 + 583	*518 ± 8*	*19.1 ± 0.1*	*179.8 ± 0.1*	1160 ± 60	29.3 ± 2.0	167.1 ± 1.7	810 ± 40	18.5 ± 1.1	158.6 ± 1.7	
0840+132				710 ± 40	13.0 ± 1.3	13.3 ± 2.7	670 ± 30	18.1 ± 1.7	166.8 ± 2.1	
0841 + 708	1610 ± 30	63.3 ± 1.2	96.3 ± 0.2	1650 ± 80	55.7 ± 2.5	111.9 ± 1.3	2020 ± 100	52.0 ± 2.1	118.0 ± 1.1	
0854 + 201	*3910 ± 290*	*98.9 ± 0.2*	*79.9 ± 0.0*	3020 ± 150	96 ± 5	178.1 ± 0.5	2620 ± 130	116 ± 6	178.3 ± 0.3	
0902 − 142	1383 ± 28	66.7 ± 1.6	84.7 ± 0.2	581 ± 30	10.2 ± 1.7†	57 ± 4	356 ± 18	10.5 ± 1.7†	102 ± 4	
0907 − 203				338 ± 17	17.0 ± 2.6†	14 ± 6	96 ± 17	<10	–	25
0909 + 013	1295 ± 26	63.9 ± 1.0	112.3 ± 0.4	1400 ± 70	36.2 ± 2.1	139.5 ± 1.6	1260 ± 60	23.8 ± 1.5	153.3 ± 1.7	
0909 + 428				970 ± 50	25.1 ± 1.9	126.2 ± 1.6	740 ± 40	32.9 ± 2.0	146.3 ± 1.8	
0914 + 028	1194 ± 24	44.7 ± 0.8	104.6 ± 0.4	840 ± 40	25.8 ± 1.8	119.7 ± 2.5	581 ± 29	20.2 ± 1.5	119.7 ± 2.4	
0918 − 120	2460 ± 120	121.3 ± 2.3	101.8 ± 0.4	500 ± 40	52 ± 3	125.8 ± 1.7	39 ± 7	<10	–	26
0920 + 446	1373 ± 27	31.6 ± 0.5	162.6 ± 0.4	2180 ± 110	25.4 ± 2.2	126.3 ± 2.0	1960 ± 100	30.1 ± 1.9	93.3 ± 2.5	
0921 − 263	2090 ± 40	7.5 ± 0.3	172.5 ± 1.1	1190 ± 60	30 ± 3	78.8 ± 2.9	660 ± 30	14.3 ± 1.9	165 ± 4	27
0927 + 390	*8456 ± 13*	*195.7 ± 0.4*	*130.2 ± 0.0*	9000 ± 450	315 ± 14	148.6 ± 1.0	5670 ± 290	212 ± 9	148.4 ± 1.1	28
0948 + 406	1910 ± 40	90.6 ± 1.7	35.2 ± 0.3	1590 ± 80	48.4 ± 2.5	18.3 ± 1.5	1110 ± 60	29.0 ± 1.5	22.9 ± 1.5	
0955 + 695	1000 ± 30	19.1 ± 0.5	40.2 ± 0.4	270 ± 20	<10	–	61 ± 6	<10	–	29
0958 + 473	1498 ± 30	38.6 ± 0.6	19.5 ± 0.5	970 ± 50	10.1 ± 1.1	150.0 ± 3.0	585 ± 29	7.0 ± 1.1	156 ± 5	
1014 − 231	–	–	–	–	–	–	–	–	–	30
1037 − 295				–	–	–	–	–	–	31
1038 + 051	*491.8 ± 0.3*	*4.0 ± 0.2*	*143.4 ± 1.4*	1180 ± 60	99 ± 7	50 ± 7	700 ± 40	72 ± 4	176.4 ± 0.6	
1041 + 061	1530 ± 30	71.6 ± 1.3	80.1 ± 0.3	1150 ± 60	20.4 ± 1.8	36.3 ± 2.8	600 ± 30	12.6 ± 1.9	34.1 ± 2.7	
1047 − 191	1166 ± 23	31.4 ± 0.6	75.8 ± 0.4	–	–	–	–	–	–	32
1047 + 717	1215 ± 24	32.5 ± 0.7	37.3 ± 0.3	1370 ± 70	32.9 ± 2.1	159.9 ± 1.8	1140 ± 60	31.1 ± 1.9	146.5 ± 1.4	
1058 + 015	*3853.1 ± 0.4*	*46.9 ± 0.1*	*122.4 ± 0.1*	4370 ± 220	347 ± 16	125.2 ± 0.7	3340 ± 170	335 ± 14	123.4 ± 0.7	
1118 − 125				–	–	–	–	–	–	33
1127 − 189	2250 ± 50	69.4 ± 1.4	84.2 ± 0.3	1630 ± 80	<10	–	830 ± 40	<10	–	34
1130 − 148	2970 ± 60	109.5 ± 2.4	131.6 ± 0.1	1460 ± 70	56 ± 9	167.8 ± 2.8	561 ± 28	29 ± 4	158 ± 4	35
1130 + 382	*882.5 ± 0.8*	*2.5 ± 0.2*	*44.7 ± 2.7*	1090 ± 50	23.2 ± 1.6	127.3 ± 1.7	660 ± 30	17.6 ± 1.2	118.6 ± 2.1	
1153 + 495	1064 ± 23	28.3 ± 0.7	90.6 ± 0.2	990 ± 50	10.1 ± 1.2	14 ± 3	650 ± 30	12.6 ± 1.9	26 ± 5	
1155 + 810	1464 ± 29	35.1 ± 0.6	74.0 ± 0.4	930 ± 50	22.2 ± 2.4	86.0 ± 2.3	564 ± 28	17.3 ± 2.8	74 ± 5	36
1159 + 292	*1232.8 ± 0.1*	*7.7 ± 0.1*	*167.3 ± 0.2*	2580 ± 130	41 ± 7	153 ± 6	2260 ± 110	64.9 ± 2.7	160.8 ± 1.1	
1209 − 240	576 ± 12	16.6 ± 0.6	170.2 ± 0.7	445 ± 23	<10	–	373 ± 19	<10	–	
1215 − 174				1630 ± 80	61 ± 5	74.1 ± 2.1	1240 ± 60	66 ± 3	60.8 ± 1.2	
1219 + 058	340 ± 7	2.2 ± 0.6	76 ± 7	381 ± 19	<10	–	222 ± 11	<10	–	37
1229 + 020	31730 ± 810	1560 ± 30	134.2 ± 0.1	24510 ± 1230	1130 ± 60	137.1 ± 0.4	15280 ± 760	920 ± 40	126.3 ± 0.6	38
1230 + 123				3190 ± 320	70 ± 15	2 ± 4	1490 ± 70	46 ± 5	158.9 ± 3.0	39
1239 + 074	876 ± 18	47.4 ± 1.0	138.4 ± 0.6	690 ± 30	55 ± 4	127.8 ± 1.1	423 ± 21	29.7 ± 2.5	114.8 ± 2.3	
1246 − 257	871 ± 18	24.0 ± 0.4	22.1 ± 0.5	830 ± 40	19 ± 26	54 ± 14	760 ± 40	32.7 ± 2.5	43.5 ± 1.6	
1256 − 057	13950 ± 280	648 ± 9	70.4 ± 0.4	16800 ± 850	760 ± 40	49.3 ± 0.6	–	–	–	40
1258 − 223				700 ± 40	15 ± 13†	27 ± 19	578 ± 29	11.5 ± 2.8†	61 ± 6	41
1258 − 319				980 ± 50	104 ± 16	70 ± 5	573 ± 29	60 ± 4	56.2 ± 1.4	
1310 + 323	*2277.1 ± 0.4*	*15.3 ± 0.1*	*23.4 ± 0.1*	2110 ± 110	59.2 ± 2.9	31.6 ± 1.1	2330 ± 120	103 ± 5	41.2 ± 0.7	
1316 − 336	1820 ± 40	80.2 ± 1.5	168.1 ± 0.4	–	–	–	1730 ± 90	65 ± 8	118 ± 5	42
1330 + 250				960 ± 50	25.8 ± 1.9	0.8 ± 1.8	556 ± 28	14.1 ± 1.3	5.4 ± 1.8	
1331 + 305	5210 ± 100	717 ± 12	33.0 ± 0.3	2520 ± 130	306 ± 13	32.7 ± 0.8	1480 ± 70	194 ± 8	32.6 ± 0.8	43
1332 + 020	556 ± 11	16.8 ± 0.4	177.7 ± 0.4	800 ± 40	5.5 ± 1.3†	162 ± 6	890 ± 40	13.6 ± 1.5†	61 ± 3	
1336 − 339	90 ± 3	<10	–	22 ± 6	<10	–	8 ± 3	<10	–	44
1337 − 129				5850 ± 290	164 ± 8	42.5 ± 0.5	5470 ± 270	178 ± 7	29.0 ± 1.0	
1347 + 123				1130 ± 60	14.4 ± 1.7	113 ± 3	760 ± 40	18.7 ± 1.4	17.3 ± 1.8	
1354 − 106	884 ± 18	48.5 ± 0.8	152.7 ± 0.4	750 ± 40	17.3 ± 2.0	36 ± 4	650 ± 30	8.0 ± 1.6	15 ± 5	
1356 + 193	1820 ± 40	54.6 ± 1.2	46.9 ± 0.2	2070 ± 100	32.8 ± 1.9	69.0 ± 1.6	1680 ± 80	38.5 ± 2.1	79.3 ± 1.0	
1408 − 078	811 ± 16	42.9 ± 0.8	166.2 ± 0.4	770 ± 40	13.5 ± 1.5†	66 ± 3	640 ± 30	18.5 ± 1.4†	24.9 ± 2.1	45

Table 2 – *continued*

	X band			*K* band			*Q* band			
	I (mJy)	*P* (mJy)	Angle (°)	*I* (mJy)	*P* (mJy)	Angle (°)	*I* (mJy)	*P* (mJy)	Angle (°)	
1419 + 383	283 ± 6	7.2 ± 0.3	46.7 ± 1.0	249 ± 13	<10	–	209 ± 17	<10	–	
1427 − 330	31.7 ± 1.9	1.0 ± 0.2	173 ± 7	–	–	–	4.4 ± 1.9	<10	–	46
1446 − 163	574 ± 11	14.5 ± 0.3	153.8 ± 0.5	323 ± 16	12.6 ± 1.5	88 ± 3	196 ± 10	7.6 ± 1.9	62 ± 9	
1458 + 716				1090 ± 50	31.9 ± 2.6	49.3 ± 1.4	690 ± 40	17.0 ± 1.5	40.5 ± 2.1	
1504 + 105	1540 ± 30	53.7 ± 0.8	155.9 ± 0.4	1750 ± 90	32.3 ± 1.9	105.0 ± 1.8	1700 ± 90	56.7 ± 2.4	72.9 ± 1.1	
1506 − 167				870 ± 40	<10	–	650 ± 30	<10	–	
1510 − 057	1730 ± 40	18.8 ± 0.3	109.9 ± 0.5	1190 ± 60	50.5 ± 2.8	86.7 ± 0.7	840 ± 40	40.7 ± 2.0	78.0 ± 1.1	
1512 − 090	2880 ± 60	15.7 ± 0.4	117.4 ± 0.7	3060 ± 150	93 ± 5	112.1 ± 1.5	2560 ± 130	80 ± 3	114.6 ± 1.1	
1513 − 100	1121 ± 22	44.9 ± 2.3	157.5 ± 1.5	1220 ± 60	36.2 ± 2.6	154.2 ± 1.9	1080 ± 50	18.8 ± 1.4	154.6 ± 2.1	
1516 + 002	*954.6 ± 1.0*	*3.9 ± 0.2*	*106.4 ± 1.6*	910 ± 50	18 ± 3	58 ± 7	870 ± 40	17.9 ± 1.5	50.6 ± 1.9	
1517 − 243				2150 ± 110	87 ± 5	46.0 ± 0.8	1940 ± 100	68 ± 3	33.7 ± 1.0	
1540 + 147	1610 ± 30	169.5 ± 2.5	154.8 ± 0.4	1270 ± 60	125 ± 6	142.5 ± 0.6	1000 ± 50	99 ± 5	140.5 ± 0.5	
1549 + 026	*975.2 ± 0.8*	*5.6 ± 0.1*	*50.6 ± 0.5*	2420 ± 120	67 ± 7	61 ± 5	2170 ± 110	73 ± 4	51.2 ± 0.6	
1550 + 054	3300 ± 70	240 ± 4	144.9 ± 0.3	2710 ± 140	180 ± 9	141.3 ± 0.5	2170 ± 110	139 ± 7	139.8 ± 0.4	
1608 + 104	1497 ± 30	21.7 ± 0.5	161.7 ± 0.6	1260 ± 60	12.7 ± 1.3†	74.9 ± 2.6	980 ± 50	12.5 ± 1.0†	65.7 ± 2.4	47
1613 + 342	*3060 ± 130*	*86.8 ± 0.4*	*4.8 ± 0.0*	2610 ± 130	38.7 ± 2.4	25.2 ± 1.8	1680 ± 80	22.5 ± 1.6	36.3 ± 2.6	
1633 + 824	781 ± 16	13.6 ± 0.3	110.3 ± 0.6	820 ± 40	<10	–	–	–	–	48
1635 + 381	2770 ± 60	96.9 ± 1.9	52.5 ± 0.2	2770 ± 140	23.3 ± 1.8	53.0 ± 1.5	2670 ± 130	56.5 ± 2.4	64.6 ± 1.2	
1638 + 573	*1356 ± 7*	*27.5 ± 0.1*	*125.7 ± 0.1*	2210 ± 110	12.8 ± 1.5	98 ± 5	1880 ± 90	22.2 ± 2.4	88.5 ± 1.4	
1642 + 398	*5653.8 ± 1.9*	*238.5 ± 0.5*	*24.8 ± 0.1*	4540 ± 230	79 ± 4	38.9 ± 0.8	4200 ± 210	77 ± 4	48.9 ± 0.5	49
1642 + 689				4660 ± 230	54 ± 4	148.0 ± 2.1	4670 ± 230	270 ± 11	103.2 ± 0.8	
1651 + 049	1630 ± 90	195 ± 5	26.7 ± 0.7	231 ± 18	<10	–	18.3 ± 2.6	<10	–	50
1654 + 396	1311 ± 26	36.5 ± 0.6	14.3 ± 0.4	1020 ± 50	33.4 ± 2.2	138.0 ± 1.1	860 ± 40	22.9 ± 1.6	140.9 ± 1.9	
1657 + 479	743 ± 15	8.8 ± 0.2	71.5 ± 0.7	670 ± 30	15.1 ± 0.7	148.5 ± 1.3	630 ± 30	12.9 ± 0.8	135 ± 8	
1658 + 077	*917.9 ± 0.4*	*16.5 ± 0.1*	*153.0 ± 0.1*	1800 ± 90	92 ± 10	113.6 ± 2.8	1590 ± 80	82 ± 3	114.1 ± 1.1	
1734 + 389	955 ± 19	6.1 ± 0.3	3.2 ± 1.1	1230 ± 60	67.7 ± 2.8	107.1 ± 1.1	1220 ± 60	98 ± 4	101.5 ± 0.8	
1740 + 522	*1357.8 ± 0.6*	*15.9 ± 0.1*	*21.1 ± 0.2*	910 ± 50	15.6 ± 1.4	151.8 ± 2.5	730 ± 40	20.9 ± 1.3	160.3 ± 1.8	
1753 + 288	*518.8 ± 1.0*	*27.1 ± 0.1*	*162.1 ± 0.1*	1740 ± 90	62 ± 5	156.6 ± 2.4	1380 ± 70	38.6 ± 1.7	157.4 ± 1.3	
1800 + 784	3000 ± 60	118.2 ± 1.7	111.7 ± 0.4	2940 ± 150	115 ± 5	99.9 ± 0.8	2380 ± 120	98 ± 5	97.2 ± 0.6	
1801 + 440	1329 ± 27	62.4 ± 1.2	49.9 ± 0.2	1350 ± 70	44 ± 9	44.2 ± 0.5	1300 ± 70	27.7 ± 1.9	48.5 ± 2.6	
1806 + 698	1720 ± 40	59.3 ± 1.0	151.4 ± 0.4	1620 ± 80	7.5 ± 1.3	147 ± 4	1460 ± 70	8.4 ± 1.1	30 ± 4	51
1824 + 568	1385 ± 28	50.4 ± 1.0	33.2 ± 0.3	1450 ± 70	111 ± 4	19.4 ± 1.1	1230 ± 60	116 ± 5	15.4 ± 0.9	
1829 + 487	3370 ± 80	71.2 ± 1.2	63.2 ± 0.4	2510 ± 130	50.2 ± 2.6	101.1 ± 1.1	1750 ± 90	57 ± 3	91.8 ± 0.5	52
1842 + 681	1640 ± 30	88.8 ± 1.6	9.9 ± 0.3	1650 ± 80	100 ± 4	15.9 ± 1.0	1440 ± 70	74 ± 4	8.3 ± 0.7	
1849 + 670	1487 ± 30	34.0 ± 0.7	143.9 ± 0.4	2120 ± 110	10.5 ± 1.3†	117 ± 4	2100 ± 100	32.4 ± 1.5†	155.4 ± 1.3	53
1850 + 283	1493 ± 30	31.2 ± 0.6	23.4 ± 0.5	840 ± 40	<10	–	432 ± 22	<10	–	
1902 + 318	1590 ± 30	50.5 ± 1.0	44.2 ± 0.2	990 ± 50	14.6 ± 1.2	27.9 ± 2.4	660 ± 30	14.0 ± 1.2	43.2 ± 2.0	
1923 − 210				1520 ± 80	31 ± 4	134.1 ± 1.4	1450 ± 70	16 ± 5	9 ± 10	
1924 − 292	11920 ± 240	224 ± 4	147.0 ± 0.3	13670 ± 680	1010 ± 50	84.9 ± 0.4	12870 ± 640	1150 ± 50	81.4 ± 0.6	
1927 + 613	1035 ± 21	65.9 ± 1.2	126.6 ± 0.2	810 ± 40	38.6 ± 2.0	112.4 ± 1.5	583 ± 29	27.2 ± 1.8	96.5 ± 1.6	
1927 + 739	3220 ± 60	44.3 ± 0.7	117.8 ± 0.4	2820 ± 140	43.3 ± 2.2	67.4 ± 1.4	2230 ± 110	50.9 ± 2.6	54.5 ± 1.3	
1939 − 154	789 ± 16	12.8 ± 0.2	157.0 ± 0.5	720 ± 40	6.8 ± 1.4†	62 ± 6	509 ± 25	7.4 ± 1.1†	30 ± 3	
2000 − 178	2040 ± 40	72.9 ± 1.2	148.8 ± 0.4	2010 ± 100	15.9 ± 2.1†	62 ± 4	1790 ± 90	26.8 ± 1.7†	18.3 ± 1.8	54
2011 − 157	2080 ± 40	46.0 ± 1.1	149.7 ± 0.9	1810 ± 90	37 ± 10	125 ± 3	1360 ± 70	22.1 ± 2.9	95 ± 8	
2022 + 616	*3028.5 ± 1.2*	*0.0 ± 0.1*	*180 ± 70*	1810 ± 90	6.9 ± 1.3	59 ± 5	1000 ± 50	6.5 ± 1.1	51 ± 5	
2101 + 037	831 ± 17	41.0 ± 0.8	130.7 ± 0.2	720 ± 40	33.6 ± 1.8	115.5 ± 1.5	620 ± 30	13.5 ± 1.3	102.3 ± 2.6	
2123 + 056	1910 ± 40	56.6 ± 1.2	5.2 ± 0.2	1460 ± 70	82 ± 3	28.1 ± 1.0	1120 ± 60	69.2 ± 2.6	21.0 ± 1.1	
2131 − 121				1980 ± 100	41.5 ± 2.9	149.4 ± 1.6	1600 ± 80	35.9 ± 2.1	174.3 ± 1.2	
2134 − 019				2040 ± 100	162 ± 8	91.0 ± 0.2	1620 ± 80	130 ± 5	72.4 ± 1.0	
2136 + 006	*7549 ± 12*	*44.7 ± 0.4*	*161.7 ± 0.2*	5220 ± 260	134 ± 5	18.0 ± 1.0	3180 ± 160	61 ± 3	0.8 ± 0.4	
2139 + 144	*2515.8 ± 0.7*	*14.2 ± 0.1*	*32.1 ± 0.2*	2110 ± 110	38 ± 9	19 ± 5	1310 ± 70	40.8 ± 2.2	172.8 ± 1.0	
2143 + 176	561 ± 11	9.7 ± 0.5	142.4 ± 0.8	690 ± 30	24.3 ± 2.0	11.4 ± 1.7	620 ± 30	17.4 ± 1.9	13.7 ± 2.1	
2148 + 069	6220 ± 120	122.2 ± 2.3	126.2 ± 0.3	5250 ± 260	95 ± 4	66.3 ± 1.2	4690 ± 230	54.5 ± 2.9	41.9 ± 1.4	
2151 − 304	1750 ± 40	39.4 ± 0.6	67.5 ± 0.4	1740 ± 90	35 ± 4	30.7 ± 2.6	1300 ± 70	33.0 ± 2.4	17.0 ± 1.9	
2158 − 150	1970 ± 40	71.2 ± 1.8	71.6 ± 0.7	1360 ± 70	62 ± 3	44.7 ± 0.6	1120 ± 60	61.6 ± 2.4	23.3 ± 1.1	
2202 + 422				2690 ± 130	184 ± 7	17.8 ± 1.0	2410 ± 120	180 ± 8	12.5 ± 0.8	
2203 + 173	1346 ± 27	44.7 ± 0.9	7.3 ± 0.2	1340 ± 70	67.4 ± 2.6	20.3 ± 1.1	1090 ± 50	70.5 ± 3.0	14.1 ± 0.9	
2203 + 317	2700 ± 50	46.4 ± 0.9	37.8 ± 0.2	2140 ± 110	19.1 ± 1.6	87.5 ± 1.4	1320 ± 70	44.0 ± 1.9	110.4 ± 1.2	
2206 − 186	3150 ± 60	41.6 ± 0.9	55.0 ± 0.7	1720 ± 90	60 ± 4	40.5 ± 0.9	1080 ± 50	33.1 ± 2.4	32.2 ± 1.5	
2211 + 238	1220 ± 24	66.9 ± 1.3	6.5 ± 0.2	950 ± 50	47.3 ± 2.0	27.1 ± 1.2	640 ± 30	36.1 ± 1.7	24.0 ± 1.3	
2218 − 035				1640 ± 80	15 ± 3	75 ± 9	1180 ± 60	6.9 ± 1.4	49 ± 5	
2225 − 049	7510 ± 150	161.3 ± 2.8	163.2 ± 0.4	8630 ± 430	264 ± 10	19.6 ± 1.0	7620 ± 380	204 ± 8	17.6 ± 1.0	

© 2009 The Authors. Journal compilation © 2009 RAS, MNRAS **401,** 1388–1398

Table 2 – *continued*

	X band			*K* band			*Q* band			
	I (mJy)	*P* (mJy)	Angle (°)	*I* (mJy)	*P* (mJy)	Angle (°)	*I* (mJy)	*P* (mJy)	Angle (°)	
2229 − 085	3390 ± 70	107.5 ± 2.1	139.1 ± 0.1	3040 ± 150	55 ± 3	178.1 ± 0.8	3210 ± 160	62 ± 3	7.3 ± 0.8	
2232 + 117	*3029.9 ± 2.4*	*39.1 ± 0.5*	*89.0 ± 0.2*	4860 ± 240	88 ± 4	67.9 ± 1.3	4300 ± 220	85 ± 7	92.8 ± 0.6	
2236 + 284	*2160.5 ± 0.2*	*33.7 ± 0.1*	*51.8 ± 0.1*	1330 ± 70	25.7 ± 2.0	163.9 ± 2.0	1140 ± 60	52.0 ± 2.9	175.2 ± 1.0	
2246 − 121	2420 ± 50	27.3 ± 0.7	119.9 ± 0.5	2350 ± 120	30.3 ± 2.0	2.8 ± 2.3	1980 ± 100	61.5 ± 2.5	163.7 ± 1.0	
2254 + 161	9660 ± 190	470 ± 9	176.4 ± 0.1	15520 ± 780	269 ± 19	140.9 ± 0.6	20620 ± 1030	250 ± 30	101 ± 3	55
2255 + 420	727 ± 15	15.7 ± 0.4	105.8 ± 0.9	438 ± 22	<10	–	183 ± 9	<10	–	
2258 − 279				2860 ± 140	18 ± 6	160 ± 8	3060 ± 160	77 ± 4	166.4 ± 1.4	56
2330 + 109	*1018.4 ± 0.1*	*16.4 ± 0.1*	*38.6 ± 0.1*	770 ± 40	23.4 ± 1.8	45.5 ± 1.0	590 ± 30	4.9 ± 1.3	28 ± 7	
2331 − 159				690 ± 30	50 ± 3	72.6 ± 1.8	524 ± 26	32.3 ± 1.7	69.4 ± 1.6	
2334 + 075	1137 ± 23	41.2 ± 0.8	146.2 ± 0.3	1490 ± 70	42.8 ± 2.7	141.4 ± 0.8	1320 ± 70	54.9 ± 2.5	149.2 ± 1.1	
2346 + 094	1281 ± 26	45.2 ± 0.9	130.5 ± 0.2	980 ± 50	30.4 ± 2.1	150.3 ± 1.7	640 ± 30	21.7 ± 1.3	154.0 ± 1.7	
2348 − 165	1590 ± 30	10.6 ± 0.3	76.7 ± 0.8	1990 ± 100	28.1 ± 2.3	16.4 ± 2.5	2230 ± 110	51.3 ± 2.2	158.8 ± 1.2	
2354 + 458	1253 ± 25	17.0 ± 0.5	176.9 ± 0.3	770 ± 40	10.1 ± 1.5	101 ± 4	392 ± 20	<10	–	
2358 − 102	1202 ± 24	31.0 ± 0.6	122.8 ± 0.3	980 ± 50	15.7 ± 3.0	32 ± 5	820 ± 40	21.7 ± 2.2	17 ± 4	

Notes. Fluxes in italics are from CLASS, in the case of multiple observations using the one with the lowest error in polarized flux density. A dagger indicates that the measurement has been taken from the Q and U maps, rather than the fits to the $u - v$ data (see text for details). A 'zero' error means smaller than 1 mJy. Other related notes: (1) Nearest plausible ID is 4C+25.01 (00 19 39.21 +26 02 45.4) which is 0.5 Jy at 1.4 GHz (NVSS); multiple sources may contribute to the *WMAP* flux density. The NVSS position was observed, leading to the detection of a resolved, polarized source at *X* band. (2) Source is identified with 3C20 which is a 50 arcsec steep-spectrum double (Laing 1981). Nearly all structure is resolved out by these observations. (3) Identification is the star-forming galaxy NGC253. Structure is nearly resolved out by these observations. (4) No *X*-band polarization available from CLASS. (5) Identification is 3C33 which is a 5 arcmin steep spectrum double (e.g. Leahy & Perley 1991). Only the central regions are seen in these observations. (6) Used as the zero-polarization calibrator at *X* band. (7) Offset polarized component? Fit to the *K*-band images gives 13.4 mJy polarized flux density at 11°. No significant difference between methods at *Q* band. (8) CLASS *X*-band polarization measured on two occasions: 21 mJy in PA 57 (total flux density 1039 mJy), 29 mJy in PA 25 (total flux density 1061 mJy). (9) Identification is the pair of sources 3C 66A, 3C 66B. Observation pointed at 3C 66A and structure heavily resolved; most of the high-frequency contribution to the flux is probably from 3C 66B, however. (10) No *X*-band polarization available. *K*-band polarization from fitting to $u - v$ data probably underestimated; images give 10.2 mJy in PA 25°. (11) Source is identified with 3C78 (e.g. Saikia et al., 1986b); heavily resolved by these observations. (12) Identified with 3C84; used as zero-polarization calibrator for *K*- and *Q*-band observations. Polarization level difficult to measure because of residual errors; best guess from analysis of images is 13 mJy polarized flux density in PA 129°. (13) Identified with 3C98 which is a 216 arcsec steep spectrum double (e.g. Leahy et al. 1997); heavily resolved by these observations. (14) Probably resolved; peak in the *Q*-band image has a polarized flux density of 11 mJy at PA 0°. (15) Extreme discrepancy between flux observed in all VLA bands and the *WMAP* flux. No obvious identification from NVSS; the observed position (04 24 2.58 +02 26 42) is the closest NVSS source (about 10 arcmin) from the *WMAP* position; *WMAP* flux may be a combination of this and two other ∼1 Jy sources at only slightly larger distance. (16) Fits to *K*-band image suggest 12 mJy polarized flux density in PA 117°, but sparse data make estimation difficult. (17) Blended source (see note in Wright et al. 2009). (18) ID is a planetary nebula (IC0418). (19) Several *X*-band measurements from CLASS with highly variable polarized flux density and PA. (20) Identification is a very large (15 arcmin) double-lobed radio source, PKS0634−20. One of the lobes was observed, and is heavily resolved. (21) Possible offset polarized component in *K* band; analysis of image suggests 10 mJy in PA 14°. (22) ID is probably the strong source 4.5 arcmin SSE, 3C196. This is a small double (e.g. Reid et al. 1995) both of whose components are detected. (23) Very little data obtained at *X* and *K* bands, no reliable results at these frequencies. (24) Phase errors limit reliability; analysis of images suggests *K*-band polarization 44 mJy at PA 23°. No significant polarization detected at *Q* band. (25) Extremely steep spectral index between *K* and *Q* bands. (26) ID is Hydra A, a large radio source (e.g. Taylor et al. 1990). Core of the source was observed, consisting of extended feature 45 arcsec across. Polarization level depends strongly on aperture used. (27) Analysis of images suggests higher *K*-band polarization (50 mJy) at same PA. (28) Identification is 4C39. (25) *X*-band polarization (CLASS) highly variable. (29) Identification is M82 (starburst galaxy). (30) Error in pointing of array. (31) Clear ID, but data of poor quality, phase solutions not good. Polarization measurements unreliable at *K* and *Q* bands. (32) Poor quality data at *K* and *Q* bands, phase solutions not good. Polarization measurements unreliable at both frequencies. (33) Most plausible ID is 4 arcmin W, little data at *K* band and phase solutions not good. (34) Good ID, poor quality data at *K* and *Q* bands, phase solutions not good and polarization measurements unreliable. (35) Good ID, poor quality data at *Q* band, phase solutions not good and polarization measurements unreliable. (36) Analysis of *Q*-band image suggests slightly lower polarized flux density, 12 mJy at PA 80°. 37. ID is 3C270; pointing position is that of the core (Birkinshaw & Davies 1985). 38. ID is 3C273; polarization at *X* band (CLASS) is high and variable. (39) ID is M87; the polarized jet pointing WNW is visible. Very little data at *K* band; this polarization measurement is unreliable. (40) Sparse data at *K* and *Q* bands; image at *Q* band suggests that this polarization measurement is unreliable. (41) Fits to *Q*-band images suggest polarized flux density of 12 mJy in PA 61°. (42) Little data at *K* band; unreliable polarization measurement at this frequency. (43) ID is 3C286; primary flux and polarization position angle calibrator; also used for non-closing offset calibration at *X* band. (44) IC4296. This is 2.5 arcmin double with compact core. No significant polarization detected. (45) Possible offset polarized component in *K* band; analysis of image suggests 14 mJy at PA 66°. (46) No obvious catalogued source. Nearest radio source is MRC 1424−328 (NVSS position 14 27 35.7, −33 02 22, 253 mJy at 1.4 GHz) approximately 1.3 arcmin E. This position yields 180 mJy of correlated flux at 8.4 GHz and no detections at higher frequencies. *WMAP* flux density of 1 Jy at 22 GHz may be the sum of a number of nearby sources. (47) Analysis of *K*-band image suggests slightly higher polarization: 13 mJy at PA 75°; detection is significant. (48) ID is NGC6251; position of core observed (e.g. Perley, Bridle & Willis 1984). (49) ID is 3C345. Phase errors in *K*-band observation; analysis of image suggests slightly higher polarized flux density of 75 mJy in PA 164°. (50) ID is Hercules A; core observed (e.g. Gizani & Leahy 2003), highly resolved. The core lies in between two polarized components, and its polarized flux density is much less than that inferred from the $u - v$ data by the automatic fitting. (51) Fits to *Q*-band images suggest polarized flux density 14 mJy in PA 60°. (52) ID is 3C380. (53) *K*-band images reveal significant detection of polarized flux density, ∼10 mJy in PA 117°. (54) Possibly offset polarized component at *K* band of 16 mJy in PA 62°. (55) ID is 3C454.3. (56) *K*-band polarization measurement unreliable; noisy map with significant phase errors.

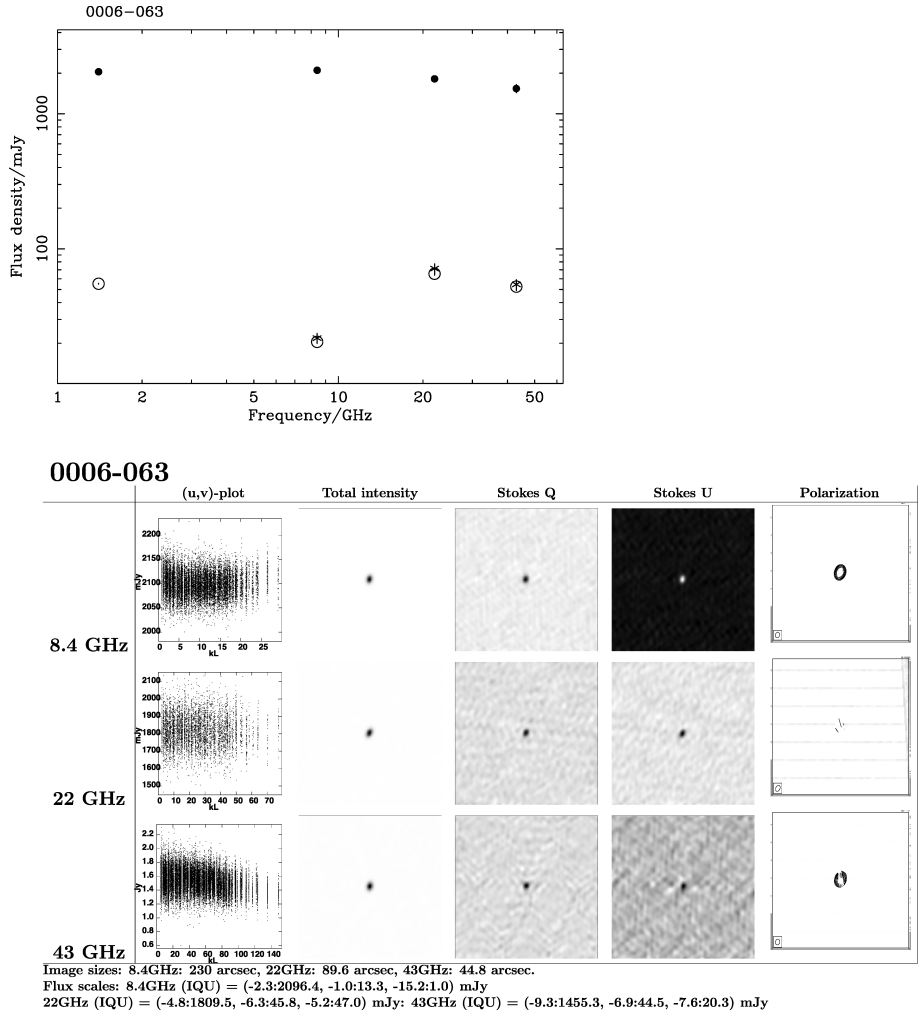


Figure 2. Full data for the first *WMAP* source, 0006−063. The spectrum (top) is given in units of log (flux density/mJy) against log (frequency/GHz); error bars are shown but are smaller than the plot symbols in many cases. Filled circles are total intensity points, and open circles are polarized flux density points measured by fitting to the (u, v) data. Stars are polarized flux density points measured by maxima from the Q, U maps. The maps of the source (bottom) include, in columns from left to right, a plot of the correlated amplitude as a function of baseline length, maps in Stokes I, Q and U, and a plot of the polarized flux vectors superimposed upon contours of Stokes I. Rows, from top to bottom, correspond to maps at 8, 22 and 43 GHz. See Supporting Information for the maps and plots of spectra for all sources.

Inspection of the images suggests that polarized flux densities of 10 mJy are likely to be significant at all frequencies in both methods.

Fig. 2 shows the complete total intensity and Stokes maps, together with the spectrum in total intensity and polarization, for the first source in order of right ascension, *WMAP* 0006−063. The other images can be found in the online material associated with this article – see Supporting Information.

3 COMPARISON WITH OTHER OBSERVATIONS

3.1 Consistency of polarization with the VLA calibrator programme

A few polarization calibrators are observed regularly by the VLA (Taylor & Myers 2000).[1] We compare the total intensity and polarization measurements of these sources with our measurements for 22 and 43 GHz in Fig. 3. Sources included in this comparison are those which were observed by the VLA in the D-configuration of 2008, interpolated if necessary to the date of our observation. Those sources which appear non-variable to 15 per cent are plotted as separate symbols; it appears that our measurements compare well with the VLA calibration programme.

[1] Online data from the VLA polarization calibration programme is available on http://www.vla.nrao.edu/astro/calib/polar/.

3.2 Comparison with *WMAP* fluxes

Ricci et al. (2006) comment that their AT20G flux densities from ATCA data on southern sources are systematically different from those of *WMAP*, in that the *WMAP* 30 GHz observations of flat spectrum sources seem to be low by a factor of about 1.2. Differences in this sense cannot be the result of resolution effects, since the larger beam of *WMAP* should result in a higher detected flux density in any resolved sources. We can investigate this with the northern hemisphere 22 GHz data presented here, and the results are shown in Fig. 4.

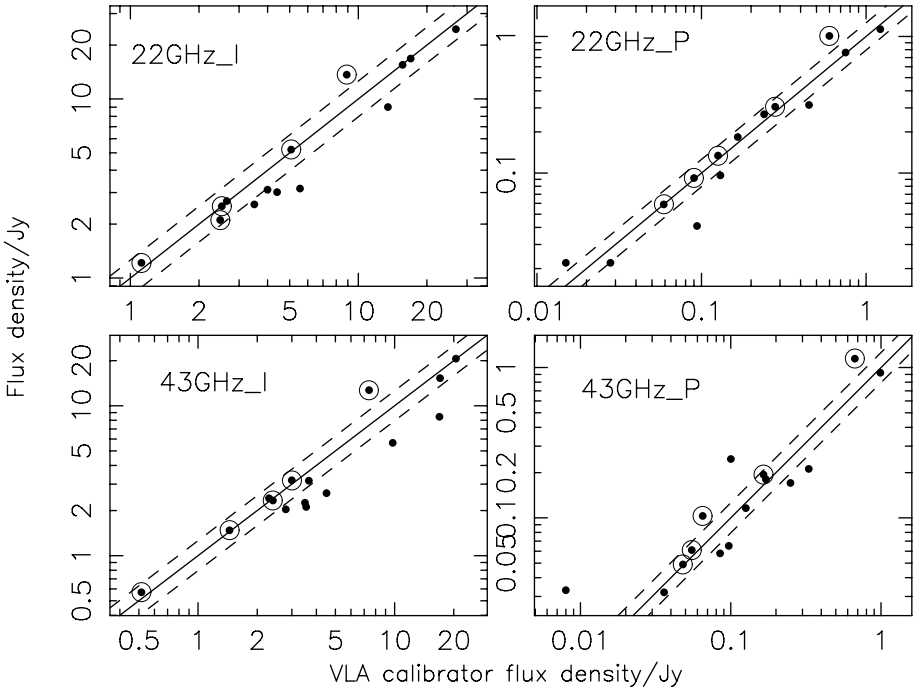


Figure 3. Comparison of intensity and polarized flux density measurements between this work and the VLA polarization calibrator monitoring programme (Taylor & Myers 2000). Sources are plotted if they were observed in the D-configuration of 2008 by the monitoring programme, interpolated to the date of our observation if necessary. Encircled points represent sources which were stable during the period 3C286, 3C48, 1310+323, 1924−292, 2136+006). Dashed lines represent variation of 20 per cent from the line of equal flux density between these observations and VLA calibration monitoring observations.

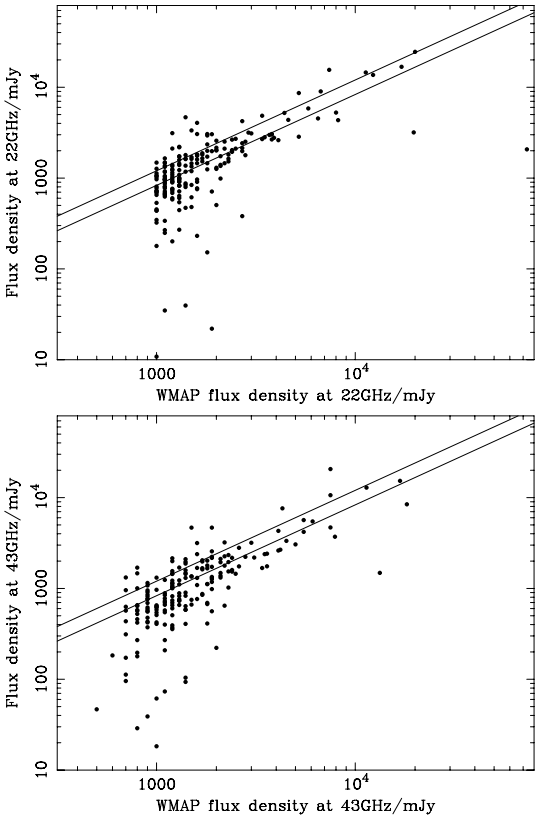


Figure 4. Comparison of the 22 and 43 GHz flux densities in this work with those of Wright et al. (2009; quoted to two significant figures in that paper). Lines are drawn at 20 per cent either side of the line of equal flux.

It is clear that there is a population of resolved sources, for which the *WMAP* flux densities at 22 and 43 GHz are higher than those of this work. A population of sources unresolved with either set of observations cluster around the line of equal flux density, although there will be some scatter induced by variability of sources between the two epochs of observation. At the 20 per cent level, there is no evidence for the flux scales being significantly different at 22 GHz. There is marginal evidence at 43 GHz for slightly lower flux densities in these observations than in the *WMAP* observations, which may be an indication that even some relatively compact sources are beginning to be resolved at this frequency. It may also be a consequence of variability bias, in which some sources which are on average just below the 1 Jy limit, happened to be in a relatively high state when observed with *WMAP*. More generally, the *WMAP* flux densities are significantly affected by CMB fluctuations, since a $\sim$50 μK fluctuation in a 30 arcmin beam corresponds to a flux density of about 100 mJy between 20–30 GHz.

3.3 Comparison with CLASS

We now compare the 8 GHz data from this project with the polarization measurements made in Cosmic Lens All-Sky Survey (CLASS) (Jackson et al. 2007), typically between 1990 and 1992, which are shown in Fig. 5 for sources with significant (6σ) polarization detections in both works. As expected, the total flux densities cluster around equal values for these point sources, but the polarized flux densities are lower for CLASS. Again, this is likely to be a resolution effect, since the CLASS observations were taken in A-configuration of the VLA, which has a maximum baseline a factor of 35 greater than that of the D-configuration used for these observations. We pick up more polarized flux in these D-configuration observations. The implication is that there is polarized emission present on arcsecond scales and therefore resolved out by CLASS. The relative degrees

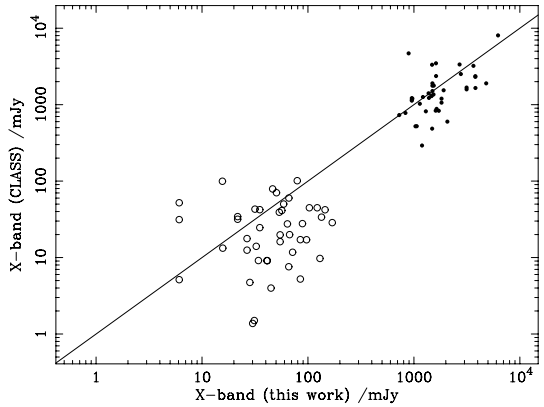


Figure 5. Comparison between flux densities in this work and CLASS of total flux density (filled circles) and polarized flux density (open circles) for cases where both surveys detect significant polarized flux. Note the generally lower polarized flux density in CLASS.

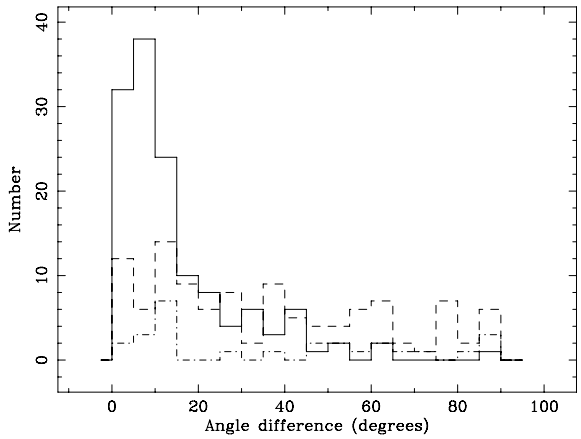


Figure 6. Differences in position angle between observed polarization at different frequencies. Solid line: difference between 22 and 43 GHz. Dashed line: difference between 8 and 22 GHz for contemporaneous observations. Dash–dotted line: difference between 8 and 22 GHz for objects where only archival CLASS 8 GHz data is available. Only observations with significant detections of polarized flux (defined as 6σ in CLASS and as objects with visible polarized flux in the Q and U maps in these observations) are plotted. Known heavily resolved sources are excluded.

of resolution of the total intensity and polarized flux indicates that the structure being resolved out is more highly polarized than that which is not.

3.4 Position angle differences and multiple components

In Fig. 6, we plot the histograms of differences in position angle between 8 and 22 GHz, and between 22 and 43 GHz, for objects with significant detections of polarization, have contemporaneous polarization measurements at all three frequencies, and have no obviously heavily resolved structure. It is obvious that the two lower frequencies are less well correlated in polarization position angle. Correlation is, unsurprisingly, slightly worse if the CLASS 8 GHz observations are used in addition to the contemporaneous 8 GHz observations. There is no obvious difference in position angle correlation between brighter and fainter sources.

The obvious interpretation of these data are that the significant Faraday rotation is present at the lower frequencies; since this effect is proportional to λ^2, the angle of rotation would be expected to be about 6–7 times larger between the lower two frequencies. Galactic Faraday rotation is unlikely to be responsible for this effect, since the <100 rad m^{-2} typical of the Galactic foreground is an order of magnitude smaller than the rotations needed significantly to affect 8 GHz measurement, and indeed in our data there is no correlation of this rotation with galactic latitude. Zavala & Taylor (2004), in a study of parsec-scale polarization of quasar radio cores, find core Rotation measures (RMs) from 500 to a few thousand rad m^{-2}, and suggest that these are due to a foreground Faraday screen close to the radio jet. Such parsec-scale components are likely to dominate the 22 and 43 GHz flux densities. On the larger scales probed by the lower frequency observations, it is possible that in many sources there are multiple polarized components with different position angles. The fact that more polarization is detected here in D-configuration than in the A-configuration CLASS observations suggests that a more extended jet component, with a lower RM than the core, may be present. Future high-sensitivity observations with e-MERLIN and the EVLA should reveal any such low surface-brightness components.

4 CONCLUSIONS

We have presented observations at 22 and 43 GHz of 199 of the 203 radio sources in the *WMAP*5 list of Wright et al. (2009) which have flux density >1 Jy at 22 GHz, and observations at 8.4 GHz of 133 of these objects. The total flux densities are broadly consistent with those listed by *WMAP*. For the few objects with previous VLA observations of polarized flux densities, there is also good agreement. There is evidence for extra polarized flux density on arcsecond scales at 8.4 GHz compared to earlier observations at higher resolution. Polarization position angles are very similar at 22 and 43 GHz, but are much less well correlated with position angles measured at 8.4 GHz. This is likely to be due to multiple polarized components which make up the generally complex radio spectra of flat-spectrum radio sources. In a further paper, we discuss correlations between the measured intensity and polarization parameters in more detail, and calculate the implications for future CMB polarization measurements of the distribution of polarized flux densities in these discrete sources.

ACKNOWLEDGMENTS

The Very Large Array, National Radio Astronomy Observatory, is a facility of the National Science Foundation operated under cooperative agreement by Associated Universities, Inc.

REFERENCES

Baars J. W. M., Genzel R., Pauliny-Toth I. I. K., Witzel A., 1977, A&A, 61, 99
Birkinshaw M., Davis R. L., 1985, ApJ, 291, 32
Blandford R. D., Rees M. J., 1978, Phys. Scripta, 17, 265
Condon J. J., Cotton W. D., Greisen E. W., Yin Q. F., Perley R. A., Taylor G. B., Broderick J. J., 1998, AJ, 115, 1693
Dickinson C. et al., 2004, MNRAS, 353, 732
Gawronski M. S. et al., 2009, MNRAS, submitted (astro-ph/0909.1189)
Gizani N. A. B., Leahy J. P., 2003, MNRAS, 342, 399
Högbom J. A., 1974, A&AS, 15, 417
Jackson N., Battye R. A., Browne I. W. A., Joshi S., Muxlow T. W. B., Wilkinson P. N., 2007, MNRAS, 376, 371
Laing R. A., 1981, MNRAS, 195, 261
Leahy J. P., Perley R. A., 1991, AJ, 102, 537

Leahy J. P., Black A. R. S., Dennett-Thorpe J., Hardcastle M. J., Komissarov S., Perley R. A., Riley J. M., Scheuer P. A. G., 1997, MNRAS, 291, 20
Mason B. S. et al., 2003, ApJ, 591, 540
Mason B. S., Weintraub L. C., Sievers J. L., Bond J. R., Myers S. T., Perason T. J., Readhead A. C. S., Shepherd M. C., 2009, ApJ, 704, 1433
Massardi M. et al., 2008, MNRAS, 384, 775
Montroy T. E. et al., 2006, in Stepp L. M., ed., Proc. SPIE, Vol. 6267, Ground-Based and Airborne Telescopes. SPIE, Bellingham, p. 62670R
Orr M. J. L., Browne I. W. A., 1982, MNRAS, 200, 1067
Perley R. A., Bridle A. H., Willis A. G., 1984, ApJS, 54, 291
Reid A., Shone D. L., Akujor C. E., Browne I. W. A., Murphy D. W., Pedelty J., Rudnick L., Walsh D., 1995, A&AS, 110, 213
Ricci R., Prandoni I., Gruppioni C., Sault R. J., DeZotti G., 2004, A&A, 415, 549
Ricci R., Prandoni I., Gruppioni C., Sault R. J., deZotti G., 2006, A&A, 445, 465
Sadler E. M., Ricci R., Ekers R. D., Sault Robert J., Jackson C. A., deZotti G., 2008, MNRAS, 385, 1656
Saikia D. J., Kulkarni V. K., Porcas R. W., 1986a, MNRAS, 219, 719
Saikia D. J., Subrahmanya C. R., Patnaik A. R., Unger S. W., Cornwell T. J., Graham D. A., Prabhu T. P., 1986b, MNRAS, 219, 545
Samtleben D., 2008, To be published in the Proceedings of the 43rd Rencontres de Moriond on Cosmology 2008, preprint (arXiv0806.4334)
Scheuer P. A. G., Readhead A. C. S., 1979, Nat, 277, 182
Simmons J. F. L., Stewart B. G., 1985, A&A, 142, 100
Taylor G. B., Myers S. T., 2000, VLA Scientific Memo 26. Available from NRAO or from http://www.vlba.nrao.edu/memos/sci/
Taylor G. B., Perley R. A., Inoue M., Kato T., Tabara H., Aizu K., 1990, ApJ, 360, 41
Taylor G. B., Gugliucci N. E., Fabian A. C., Sanders J. S., Gentile G., Allen S. W., 2006, MNRAS, 368, 1500
Tegmark M., Efstathiou G., 1996, MNRAS, 281, 1297
Toffolatti L., Argueso Gomez F., de Zotti G., Mazzei P F. A., Danese L., Burigana C., 1998, MNRAS, 297, 116
Toffolatti L., Negrello M., González-Nuevo J., de Zotti G., Silva L., Granato G. L., Argueso F., 2005, A&A, 438, 475
Tucci M., Martínez-González E., Toffolatti L., González-Nuevo J., de Zotti G., 2004, MNRAS, 349, 1267
Vol'Vach A. E., Vol'Vach L. N., Kardashev N. S., Larionov M. G., 2008, Astron. Rep., 52, 429.
Waldram E. M., Pooley G. G., Grainge K. J. B., Jones M. E., Saunders R. D. E., Scott P. F., Taylor A. C., 2003, MNRAS, 342, 915
Waldram E. M., Bolton R. C., Pooley G. G., Riley J. M., 2007, MNRAS, 379, 1442
Wall J. V., Jackson C. A., 1997, MNRAS, 290, L17
Wright E. L. et al., 2009, ApJS, 180, 283
Zavala R. T., Taylor G. B., 2004, ApJ, 612, 749

SUPPORTING INFORMATION

Additional Supporting Information may be found in the online version of this article:

Figure 2 (a) The complete maps. This figure includes, in columns from left to right, a plot of the correlated amplitude as a function of baseline length for each source, maps in Stokes I, Q and U, and a plot of the polarized flux vectors superimposed upon contours of Stokes I. For each object, rows are given corresponding to maps at 8, 22 and 43 GHz, respectively. (b) Plots of spectra given in units of log(flux density/mJy) against log(frequency/GHz). Filled circles are total intensity points, and open circles are polarized flux points measured by fitting to the (u, v) data. Stars are polarized flux points measured by maxima from the Q, U maps.

Please note: Wiley-Blackwell are not responsible for the content or functionality of any supporting materials supplied by the authors. Any queries (other than missing material) should be directed to the corresponding author for the article.

This paper has been typeset from a TEX/LATEX file prepared by the author.